International Journal of
Environmental Research and Public Health

MDPI

Article

Combined Effects of CO_2 Adsorption-Induced Swelling and Dehydration-Induced Shrinkage on Caprock Sealing Efficiency

Xiaoji Shang [1], Jianguo Wang [1,*], Huimin Wang [2] and Xiaolin Wang [3]

[1] State Key Laboratory for Geomechanics & Deep Underground Engineering, School of Mechanics and Civil Engineering, China University of Mining and Technology, Xuzhou 221116, China
[2] College of Water Conservancy and Hydropower Engineering, Hohai University, Nanjing 210098, China
[3] School of Engineering, University of Tasmania, Hobart 7001, Australia
* Correspondence: jgwang@cumt.edu.cn or nuswjg@yahoo.com

Abstract: Carbon dioxide (CO_2) may infiltrate into the caprock and displace brine water in the caprock layer. This causes two effects: one is the caprock swelling induced by the CO_2 adsorption and the other is the caprock dehydration and shrinkage due to CO_2–brine water two-phase flow. The competition of these two effects challenges the caprock sealing efficiency. To study the evolution mechanism of the caprock properties, a numerical model is first proposed to investigate the combined effects of CO_2 adsorption-induced expansion and dehydration-induced shrinkage on the caprock sealing efficiency. In this model, the caprock matrix is fully saturated by brine water in its initial state and the fracture network has only a brine water–CO_2 two-phase flow. With the diffusion of CO_2 from the fractures into the caprock matrix, the CO_2 sorption and matrix dehydration can alter the permeability of the caprock and affect the entry capillary pressure. Second, this numerical model is validated with a breakthrough test. The effects of the two-phase flow on the water saturation, CO_2 adsorption on the swelling strain, and dehydration on the shrinkage strain are studied, respectively. Third, the permeability evolution mechanism in the CO_2–brine water mixed zone is investigated. The effect of dehydration on the penetration depth is also analyzed. It is found that both the shale matrix dehydration and CO_2 sorption-induced swelling can significantly alter the sealing efficiency of the fractured caprock.

Keywords: CO_2 geological sequestration; brine water-CO_2 two-phase flow; matrix dehydration; caprock swelling; permeability evolution

check for updates

Citation: Shang, X.; Wang, J.; Wang, H.; Wang, X. Combined Effects of CO_2 Adsorption-Induced Swelling and Dehydration-Induced Shrinkage on Caprock Sealing Efficiency. *Int. J. Environ. Res. Public Health* **2022**, *19*, 14574. https://doi.org/10.3390/ijerph192114574

Academic Editor: Lingxin Chen

Received: 21 September 2022
Accepted: 2 November 2022
Published: 6 November 2022

Publisher's Note: MDPI stays neutral with regard to jurisdictional claims in published maps and institutional affiliations.

Copyright: © 2022 by the authors. Licensee MDPI, Basel, Switzerland. This article is an open access article distributed under the terms and conditions of the Creative Commons Attribution (CC BY) license (https://creativecommons.org/licenses/by/4.0/).

1. Introduction

The potential leakage of the stored carbon dioxide from the caprock layers is an important environmental safety issue to the CO_2 sequestration in geological formations [1,2]. The numerical simulations for the commercial-scale CO_2 sequestration projects have evaluated the migration and interaction with the storage reservoir [3,4]. These evaluations focus on the trapping mechanisms and reservoir storage capacity [5]. The trapping mechanisms of the mineral, solubility, hydrodynamics, and structure have been studied, respectively [6–9]. Further, the effective storage capacity is estimated based on the plume formation, accumulative pressure, and other factors [10,11]. The structural trapping is usually formed by many caprock layers, which are physical barriers with a low permeability to prevent the CO_2 from a further upwards migration. The CO_2 accumulates gradually from the reservoir to the bottom of the caprock layer during the sequestration process [12–14] and interacts with the caprock layer. When the accumulation pressure exceeds the initial entry capillary pressure, CO_2 gradually penetrates into the caprock layer [15,16] and the caprock sealing efficiency is impaired [17]. The leakage of CO_2 after the breakthrough of the caprock layer damages the safety of the storage reservoir. Therefore, the key issue to the CO_2 geological sequestration is the caprock sealing stability and efficiency. How the dehydration of the

shale matrix alters the sealing efficiency during the CO_2–water displacement has not been well investigated so far [8,18].

A caprock layer may be highly fractured and heterogeneous, even at the depth of 4 km [1,19]. Macropores in the fractures and micropores in the matrix make up the two-scale pore systems in a fractured caprock [16,20,21]. In these systems, the micropores in the matrix are the storage space of carbon dioxide because their extremely large internal surface area adsorbs CO_2. These micropores are small in size and fully or partially saturated in the caprock layer [8]. The main component of the caprock is shale, whose shale matrix is of a low porosity and an ultra-low permeability [22]. Closely spaced fractures are usually assumed in the modeling of the macropore system [23,24]. These fractures are the main channels for the CO_2–brine two-phase flow. Therefore, the combination of two-phase flow in the fractures, CO_2 sorption and diffusion in the matrix, and the matrix dehydration makes up the main transport mechanisms [25]. Both the CO_2 sorption and dehydration induce the swelling or shrinkage of the shale matrix and may modify the stability of the caprock sealing.

If the caprock is water saturated, the dehydration of the matrix may impact the caprock sealing efficiency. Some water-saturated minerals are fully swelled under in situ conditions [8,26]. The water saturation is changing while the CO_2 displaces the water in the matrix of the caprock. This change results in the shrinkage of the shale matrix, thus enlarges the aperture of the shale fractures and may enhance the caprock permeability [18,27]. On the other hand, some minerals such as clay may adsorb the CO_2 molecules onto their internal surfaces, thus inducing the swelling of the matrix and the closing of some fractures. The swelling of the caprock matrix is contributed by these two competitions of a dehydration-induced shrinkage and a sorption-induced swelling. The competition effects promote the self-limiting or self-enhancing change in the physical and mechanical properties of caprocks throughout the multi-physical interaction process [28]. Hence, the CO_2 sorption and dehydration in the caprock matrix are the key issues in the evaluation of the caprock sealing efficiency.

The CO_2–brine water two-phase flow in the caprock layer is a multi-physical process [29]. The mechanical deformation, the CO_2–brine two-phase flow in the fractures, the gas diffusion in the caprock matrix, and the dehydration- and sorption-induced swelling are all included in this multi-physical process. The CO_2 sorption/desorption, pore pressure, mechanical deformation or stress compaction, and geochemical reaction may be altered in these mechanical processes. The fractures are filled with the CO_2–brine water two-phase flow. The two-phase flow may stimulate the local deformation of the caprock and change the wettability of the caprock and the entry capillary pressure of the fractures [30]. In addition, the flow channels can be modified through the CO_2–rock interaction, thus altering the porosity and permeability of the caprock [18,31]. The CO_2 sorption has an important impact on the stability of the caprock sealing. The results are variable with the organic compositions, types, and shale contents [32]. Furthermore, clay minerals in shale layers can adsorb some free gas. The capacity of gas adsorption varies with the clay type, volume, and type of gas itself. The adsorbed volume of gas is closely related to the pores surface area. It is found that there are similar sorption behaviors between the coal and shale. The Langmuir formula is applicable to the shales accordingly [33]. On the other hand, some minerals swell after absorbing water (hydration) and shrink after losing water (dehydration) [19,25]. Therefore, these interactions can seriously affect the height of the CO_2 penetration upward or the efficiency of the caprock sealing, but no publication exploring this is available presently.

The combined effects of CO_2 adsorption-induced swelling and dehydration-induced shrinkage on the caprock sealing efficiency are investigated in this paper. First, a two-phase flow in the fractures, the diffusion processes for CO_2–brine water in the shale matrix, and the mechanical compaction process of fractured caprock are represented in a conceptual model. Then, the porosity and permeability constitutive models with the effect of the dehydration process are developed, respectively. The entry capillary pressure is also expressed

mathematically. These models together constitute a new coupled multi-physical model. It is an extension of our previous model for the efficiency of the caprock sealing [16,24]. Third, the effects of the adsorption-induced swelling and dehydration-induced shrinkage as well as the stress compaction are expressed in terms of the fracture aperture change. Through the finite element method, this fully coupled model is solved numerically and verified by a breakthrough test of a fractured sample. Finally, the effects of the adsorption-induced swelling and dehydration-induced shrinkage on the self-limiting or self-enhancement within a caprock layer are numerically investigated.

2. Multi-Physical Interaction Model for a Fractured Caprock Layer

2.1. Multi-Physical Interactions in a Fractured Caprock

The disturbance mechanisms of caprock sealing induced by a two-phase flow stimulation are complex. The pressure of CO_2 at the bottom of the caprock layer continuously increases with the CO_2 accumulation from the storage reservoir. If the CO_2 pressure is lower than the sum of the reservoir pressure and entry capillary pressure [34,35], the Darcy flow does not occur. This kind of sealing is called the capillary sealing. In this sealing mode, the diffusion and flow of the dissolved gas in pore water are the main means of CO_2 migration. The Darcy flow starts once the gas pressure is over the sum of the reservoir pressure and the entry capillary pressure [35]. In two-phase Darcy flow process, the CO_2 displaces the pore water in the caprock layer.

Caprocks are a mostly fractured porous media which consist of fractures and a matrix. The fracture usually has a much lower entry capillary pressure than the shale matrix. The shale caprock of water-saturated is different from the shale gas reservoir. The pore water still remains in micropores after the CO_2 penetrates into the fractures [36]. As CO_2 in the fracture network gradually diffuses into the shale matrix, water in the shale matrix will be replaced by CO_2 and then enters the fractures. These two processes are usually diffusive and called sorption and dehydration, respectively. Figure 1 presents a detailed conceptual model of these mechanisms. In this conceptual model, the CO_2–brine water two-phase flow is observed only in the fracture network. However, due to the interaction between the shale caprock and CO_2, the CO_2 adsorbs into the matrix and water is then produced due to the dehydration [37]. The matrix is subjected to the two actions of both the CO_2 adsorption-induced swelling and dehydration-induced shrinkage (see Figure 2). Therefore, the multi-physical processes can be represented by this conceptual model in various time scales: (1) a CO_2–brine water two-phase flow in the initial water-saturated fractures; (2) the propagation of gas front-induced mechanical process; (3) a CO_2 diffusion and adsorption into the caprock matrix; (4) the water dehydration of the matrix; and (5) the geochemical reactions among CO_2, water, and caprock [38]. The first three events are short term: the mechanical deformation occurs immediately when the effective stress has any change. The CO_2–brine water two-phase flow in the fracture network is instantly started when the entry capillary pressure is run over. The diffusion, dehydration, and geochemical reaction processes may be long term, such as the span of geological time [39].

2.2. Dehydration and Shrinkage of Shale Matrix

The CO_2–brine water displacement mechanism in a shale matrix block is depicted in Figure 3. Shale is a sedimentary rock formed by dewatering and the cementation of clay minerals. The clay minerals are water-sensitive [40]. The shale matrix swells when water flows into the matrix (called the hydration process). Inversely, the shale matrix shrinks when the water flows out of the matrix (called the dehydration process). Figure 3a presents a shale matrix block which is surrounded by fractures. Both the fractures and the matrix were assumed to have the same initial phase pressures of a CO_2–brine water two-phase flow. The phase pressures changed continuously with the two-phase flow process in the fracture network (see Figure 3b) and caused CO_2 to flow into the block and the water to flow out of the block.

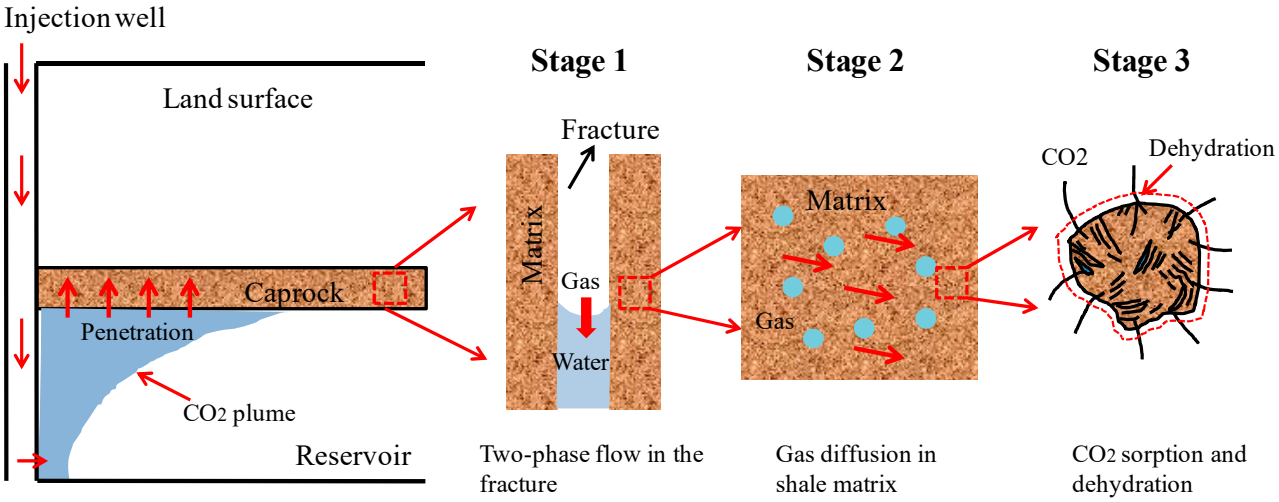

Figure 1. CO_2 transport and dehydration mechanism of shale caprock.

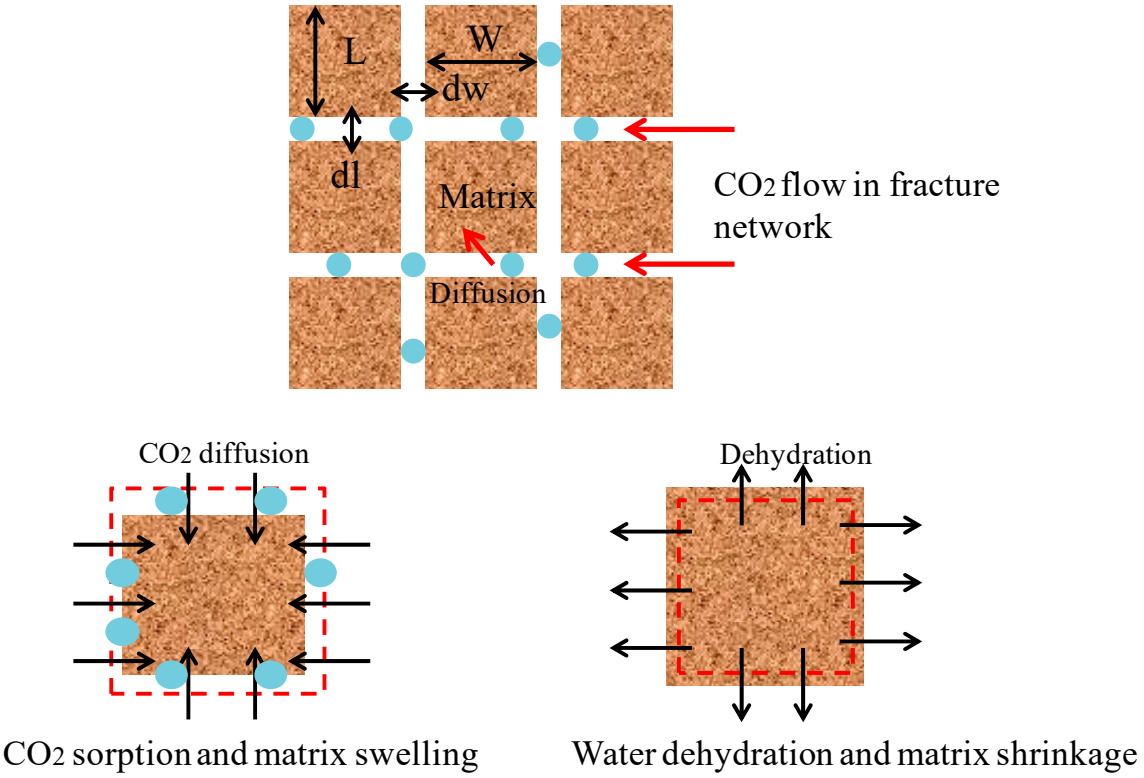

Figure 2. CO_2 sorption and dehydration model in shale caprock. The abbreviated letters L, dl, W, and dw are short for length, derivative of length, width, and derivative of width, respectively.

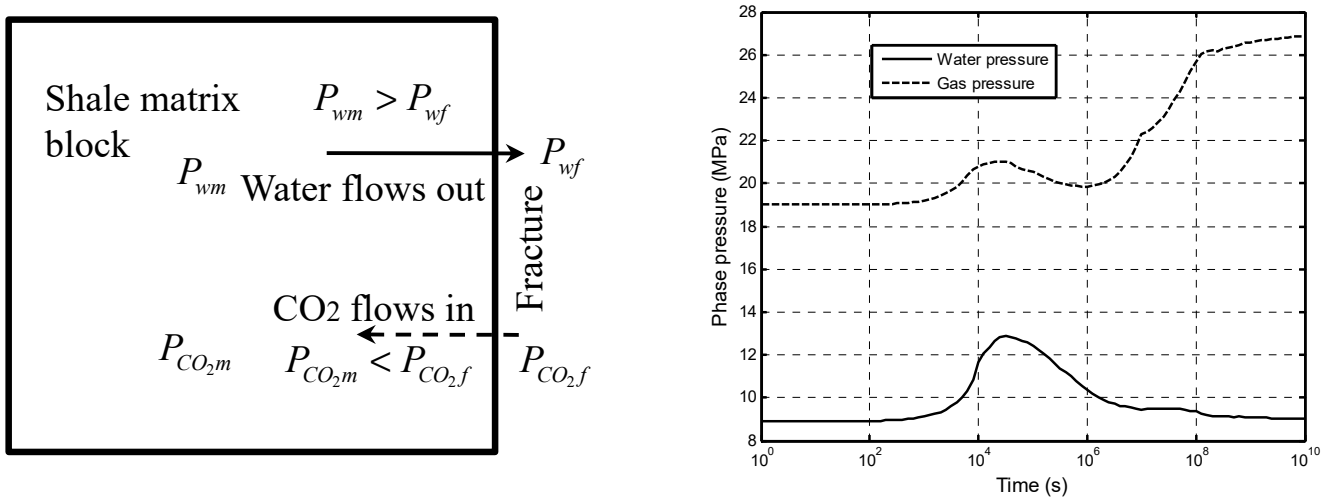

(**a**) Pressure in shale matrix (**b**) Phase pressure

Figure 3. CO_2-water displacement in tight caprock. The abbreviated letters P_{wm}, P_{wf}, P_{CO_2m}, P_{CO_2f} are short for the pressures of water in the matrix, water in the fractures, CO_2 in the matrix, and CO_2 in the fractures, respectively.

2.2.1. Water Content, Saturation, and Porosity of Shale Matrix

The porosity of shale matrix is calculated by:

$$\phi_m = \frac{V_V}{V_T} \tag{1}$$

The brine water saturation is defined as:

$$s_{wm} = \frac{V_{bw}}{V_V} \tag{2}$$

The volumetric water content W is related to the water saturation as:

$$W = \phi_m s_{bwm} \tag{3}$$

The water content (by weight) is the ratio of water mass to solid mass as:

$$W_c = \frac{M_w}{M_s} = S_{bwm} \frac{\phi_m}{1-\phi_m} \frac{\rho_{bw}}{\rho_s} \tag{4}$$

Equation (4) is a relationship among the porosity, water content, and water saturation. Obviously, any change in one factor may induce a change in the other two. Further, the water loss in the shale matrix (or the dehydration process) may be not only from free water but also from some bonding water [18]. At this time, the bonding water has the following mass [41]:

$$M_b = \left(\frac{A}{1+W_c}\right)\left(\frac{\alpha_1}{1-\alpha_1}\right) \tag{5}$$

where ϕ_m is the porosity of the shale, S_{bwm} is the water saturation in the pores, V_V is the pore volume, V_W is the water volume, and V_T is the total volume. M_{bw} is the water mass and M_S is the shale mass. ρ_{bw} is the density of the water and ρ_s is the density of the shale matrix. A and α_1 are the correction factors for the total water and bonding water content contributing to a shrinkage deformation, respectively.

This bonding water is usually regarded as a part of the solid particles. If this bonding water does not contribute to a shrinkage deformation, the water content of the shale matrix is revised as:

$$\overline{W}_c = \frac{M_{bw} - M_b}{M_s + M_b} = \frac{\rho_s}{\rho_{bw}(1 + W_c)}\left(W_c - \frac{A\alpha}{1 - \alpha}\right) \tag{6}$$

where α is the correction factor for the bonding water content not contributing to the shrinkage deformation.

2.2.2. Dehydration-Induced Volumetric Strain of Shale Matrix

This matrix shrinkage is measured by the volumetric strain ε_{vbw} through a moisture-adsorption test. A quadric function is here used for the moisture-swelling relationship as:

$$\varepsilon_{vbw}(W_c) = K_1 W_c + K_2 W_c^2 \tag{7}$$

where K_1 and K_2 are the expansion coefficients. A typical hydration-induced swelling of the Mancos shale [42] is presented in Figure 4, where $K_1 = 0.212$ and $K_2 = 33.24$. Obviously, the swelling strain of this shale is big and Equation **(7)** is able to describe this relationship.

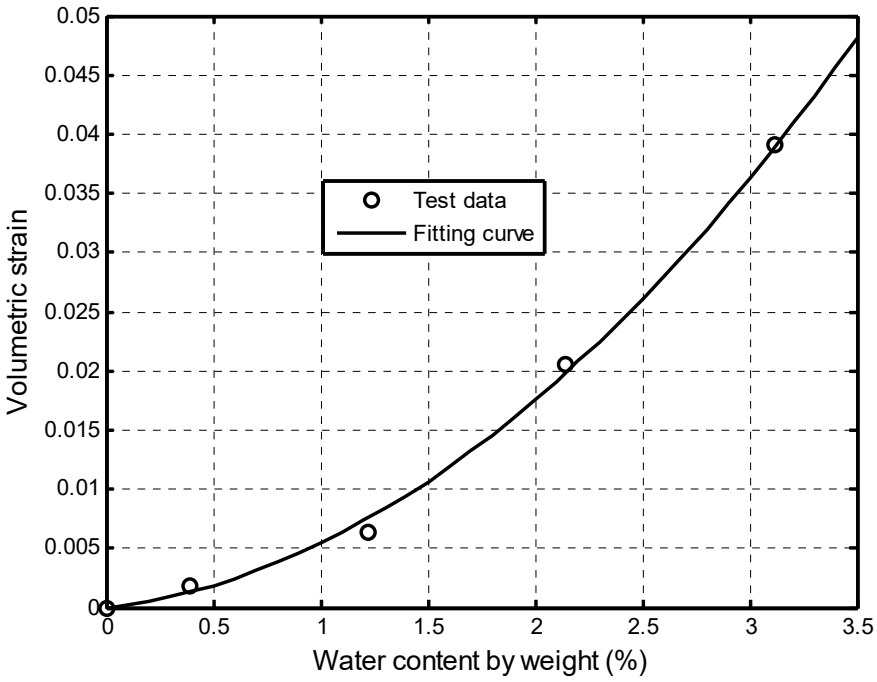

Figure 4. Hydration-induced strain in Mancos shale [42].

2.3. Dehydration-Induced Modifications for Porosity and Permeability Models

2.3.1. Porosity Evolution in Homogeneous Shale Matrix

The porosity ratio is obtained as:

$$\frac{\phi}{\phi_0} = 1 + (1 - R)\frac{S_0 - S}{1 + S} \tag{8}$$

where $R = \alpha/\phi_0$. S_0 and S are the effective volumetric strains in the initial and current state, respectively. They are defined as follows

$$S_0 = \varepsilon_{v0} + \frac{p_0}{K_s} - \varepsilon_{s0} - \varepsilon_{D0}, \quad S = \varepsilon_v + \frac{p}{K_s} - \varepsilon_s - \varepsilon_D \tag{9}$$

where ε_v and ε_{v0} are the current and initial volumetric strain, respectively, and ε_{s0} and ε_s are the initial and current volumetric strain induced by the sorption. ε_{D0} and ε_D are

the initial and current hydration-induced volumetric strain, respectively. ϕ_0 is the initial porosity and p_0 is the initial pore pressure.

2.3.2. Local Fracture Strain

Both the fractures and matrix contribute to the total deformation of the fractured shale (see Figure 5).

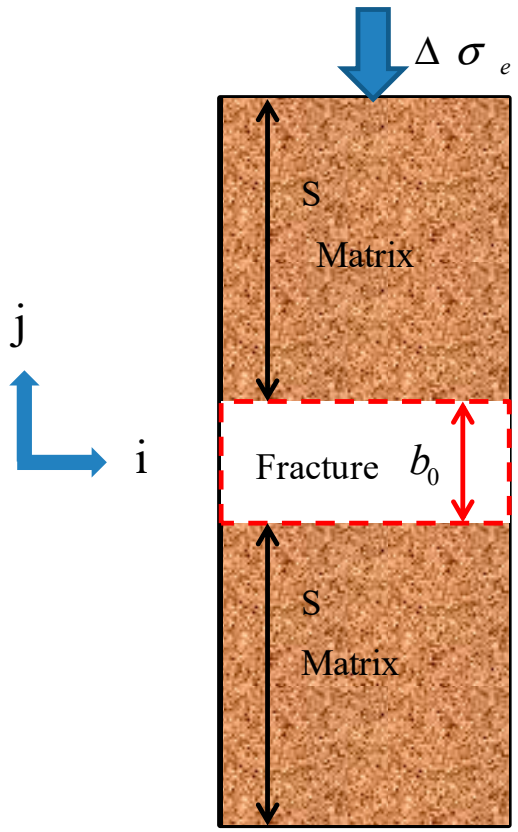

Figure 5. Deformation of fractured shale element.

The change in the fracture aperture is:

$$\Delta b = (s + b_i)\Delta\varepsilon_e - s\Delta\varepsilon_{em} \tag{10}$$

Equation (10) can be reformulated as:

$$\Delta b = b_i\left[1 + \frac{s}{b_i}\left(1 - \frac{\Delta\varepsilon_{em}}{\Delta\varepsilon_e}\right)\right]\Delta\varepsilon_e = b_i\left[1 + n\frac{1 - R_m}{\phi_{f0}}\right]\Delta\varepsilon_e \tag{11}$$

The local fracture strain is derived as:

$$\frac{\Delta b}{b_i} = \left[1 + n\frac{1 - R_m}{\phi_{f0}}\right]\Delta\varepsilon_e \tag{12}$$

where s is the fracture spacing and ϕ_{f0} is the initial fracture porosity. $b_i/s = \phi_{f0}/n$ are in an n-dimension case. ε_e is the average effective strain and $\Delta\varepsilon_e$ is its increment in a fixed representative length ($\Delta\varepsilon_e = (S_0 - S)/(1 + S)$). ε_{em} is the effective strain, and $\Delta\varepsilon_{em}$ is the increment of ε_{em}. $R_m = \Delta\varepsilon_{em}/\Delta\varepsilon_e$ is the increment strain ratio of the average effective strain to effective strain.

2.3.3. Evolution of Permeability

The initial permeability of the fracture is expressed as the following cubic law:

$$k_0 = \frac{b_i^3}{12s} \tag{13}$$

If fracture aperture b_i changes due to the compaction, swelling, dehydration or their combinations, the permeability k will change as follows:

$$k = \frac{(b_i + \Delta b)^3}{12s} \tag{14}$$

where Δb is the change in the fracture aperture.

Combining Equation (14) with Equation (13) yields the permeability ratio of the fracture as:

$$\frac{k}{k_0} = \left(1 + \left(1 + n\frac{1 - R_m}{\phi_{f0}}\right)\Delta\varepsilon_e\right)^3 \tag{15}$$

In two-dimensional space, this permeability ratio is:

$$\frac{k}{k_0} = \left[1 + \frac{2(1 - R_m)}{\phi_{f0}}\Delta\varepsilon_e\right]^3 \tag{16}$$

2.4. Change in Entry Capillary Pressure with Fracture Deformation

The caprock is initially water saturated. The entry capillary pressure (Appendix A) limits the CO_2 containment capacity of the caprock and depends on both the pore geometry in the matrix and the CO_2/brine water/rock wettability [43]. The entry capillary pressure is calculated by

$$p_e = \frac{2\sigma\cos(\theta)}{r} \tag{17}$$

where r is the pore radius. σ is the interfacial tension of water, CO_2, and caprock. θ is the contact angle to express the hydrophilic interactions.

The current aperture of a fracture is:

$$b = b_i + \Delta b \tag{18}$$

It is equivalent between the aperture of a fracture and the representative radius of a pore in this paper. In the calculation of the entry capillary pressure in a fracture, $r = b$. The entry capillary pressure of the fracture at the initial state is:

$$p_{ei} = \frac{2\sigma_i\cos\theta_i}{b_i} \tag{19}$$

Here, the subscript 'i' denotes the initial state. The interfacial tension and wettability are influenced by the pressure, temperature, or chemical reactions during CO_2–brine water–rock contacting process [36]. If these physical variables do not change with the deformation, the CO_2 entry pressure is concluded as:

$$p_e = \frac{p_{ei}}{1 + \left(1 + n\frac{1-R_m}{\phi_{f0}}\right)\Delta\varepsilon_e} \tag{20}$$

This is our new entry pressure of CO_2 after considering the effective strain.

3. Mass Transfer of Two-Phase Flow between Fractures and Shale Matrix

3.1. Mass Transfer of CO_2 between Fractures and Shale Matrix

The sorption rate of CO_2 is denoted by:

$$Q_m = -\rho_c \rho_{ga} \frac{dm_b}{dt} \tag{21}$$

where Q_m is the source term of mass and the minus sign '-' represents the mass transfer from the shale matrix to the fractures. m_b is the residual content of CO_2 in the matrix at pressure p. dm_b/dt is the exchange rate of CO_2 between the fractures and the shale matrix and is expressed as:

$$\frac{dm_b}{dt} = -\frac{1}{\tau}[m_b - m_e(p)] \tag{22}$$

where τ is the diffusion time, m_e is the gas content at the equilibrium state, and p is the pressure of the fractures.

The diffusion time is defined as:

$$\tau = \frac{1}{aD} \tag{23}$$

where a is a shape factor and D is the diffusion coefficient of CO_2 in the matrix.

3.2. Dehydration due to Water Transfer between Fractures and Shale Matrix

The dehydration of the shale matrix is still assumed to follow a diffusion process [42]. In this paper, this process is described by a simplified diffusion equation as:

$$\frac{dm_{bw}}{dt} = -\frac{1}{\tau_{bw}}[m_{bw} - m_{bwe}(s_{bw})] \tag{24}$$

where m_{bw} is the mass of the water phase in the shale matrix, and m_{bwe} is the water content at the equilibrium state with the water saturation s_{bw} in the fractures.

The diffusion time of water in the shale matrix is denoted as:

$$\tau_{bw} = \frac{1}{aC} \tag{25}$$

where C is the water diffusion coefficient in the matrix [42].

The CO_2–brine water two-phase flow displacement is complicated in a porous media [44], but can be described by following the diffusion process over spherical pellets [45]:

$$\frac{dm_{bw}}{dt} = \frac{15D_{bw}}{R_{bw}^2}[m_{bwe}(S_{bw}) - m_{bw}] \tag{26}$$

where D_{bw} is the diffusion coefficient and R_{bw} is the characteristic radius of spherical pellets. It is obvious that both Equation (**26**) and (**24**) have the same form.

4. Mathematical Descriptions of Multi-Physical Processes

4.1. Mass Conservation Laws for CO_2–Brine Water Two-Phase Flow in Fractures

The CO_2–brine water two-phase flow occurs in the fractures. CO_2 is considered as the non-wetting phase, and the brine water is considered as the wetting phase. According to the mass conservation law, the governing equations of CO_2 and brine water are obtained as follows.

For the brine water phase:

$$\frac{\partial(\phi\rho_{bw}s_{bw} + \rho_{bw}m_{bw})}{\partial t} + \nabla \cdot \left(-\frac{kk_{rbw}}{\mu_{bw}}\rho_{bw}(\nabla p_{bw} + \rho_{bw}g\nabla H)\right) = f'_{bw} \tag{27}$$

Being different from the brine water, the CO_2 has two unique features: (1) a strong compressibility in both free and supercritical states and (2) the existence of both free and absorbed phases in the fractures. Furthermore, the CO_2 diffuses from the fractures into the matrix and displaces the pore water in the shale matrix. The mass of CO_2, m_{nw}, can be derived as

$$m_{nw} = \phi\rho_{nw}S_{nw} + \rho_{nwa}\rho_c\frac{V_L p*}{p_L + p*} + \rho_{nwa}\rho_c m_b \tag{28}$$

Equation (28) shows that the storage states of the CO_2 phase include a free-phase form (the first term), an absorbed form in the fracture network (the second term), and the mass exchange from the matrix (the third term).

For the CO_2 phase:

$$\frac{\partial m_{nw}}{\partial t} + \nabla\cdot\left(-\frac{kk_{rnw}}{\mu_{nw}}\rho_{nw}(\nabla p_{nw} + \rho_{nw}g\nabla H)\right) = f'_{nw} \tag{29}$$

where ρ_{bw} is the density of the brine water. k is the absolute permeability of the shale. k_{rbw} and k_{rnw} are the relative permeabilities (Appendix B) of the brine water and CO_2 in the fracture network, respectively. The viscosity at in situ conditions is μ_w for water and μ_{nw} for CO_2. ϕ is the porosity of the fracture network. The source term is f'_w for water and f'_{nw} for CO_2. p_{bw} and p_{nw} are the pore pressures of the brine water and CO_2 in the fractures. s_{bw} and s_{nw} are the saturations of the brine water and CO_2, respectively. H is the height in the vertical direction. ρ_{nwa} and ρ_c are the densities of the CO_2 and the shale caprock under the standard conditions, respectively. g is the gravity acceleration.

The equation of the state gives the CO_2 density, ρ_{nw}, as:

$$\rho_{nw} = \frac{M_{nw}}{Z_{nw}RT_{nw}}p_{nw} = \beta p_{nw} \tag{30}$$

where M_{nw} and Z_{nw} are the molecular weight and compressibility factor of CO_2, respectively. R denotes the universal gas constant and T_{nw} is the temperature of CO_2. β is a constant of a range for the CO_2 pressure and temperature.

The pressure of CO_2, p^*_{nw}, in the fractures is:

$$p^*_{nw} = s_{nw}p_{nw} \tag{31}$$

Introducing the relationship between the capillary pressure and saturation yields the final form of two-phase flow governing equations in the fractures.

For the brine water flow:

$$\phi C_p\frac{\partial p_{nw}}{\partial t} - \phi C_p\frac{\partial p_{bw}}{\partial t} + s_{bw}\frac{\partial\phi}{\partial t} = \nabla\cdot\left[\frac{kk_{rbw}}{\mu_{bw}}(\nabla p_{bw} + \rho_{bw}g\nabla H)\right] - \frac{dm_{bw}}{dt} + f_{bw} \tag{32}$$

For the CO_2 flow:

$$\begin{aligned}&\phi'(s_{nw} - p_{nw}C_p)\tfrac{\partial p_{nw}}{\partial t} + \phi' p_{nw}C_p\tfrac{\partial p_{bw}}{\partial t} + \phi s_{nw}p_{nw}\tfrac{\partial\phi}{\partial t}\\ &= \nabla\cdot\left[\tfrac{kk_{rnw}}{\mu_{nw}}p_{nw}(\nabla p_{nw} + \rho_{nw}g\nabla H)\right] - \mathrm{p}_a\rho_c\tfrac{dm_b}{dt} + f_{nbw}\end{aligned} \tag{33}$$

The sorption modified porosity is:

$$\phi' = \phi + \rho_{nwa}\rho_c\frac{V_L p_L}{(p_L + p^*_{nw})^2} \tag{34}$$

$$\phi = \frac{\Delta b}{b_i} = \left[1 + n\frac{1 - R_m}{\phi_{f0}}\right]\Delta\varepsilon_e \tag{35}$$

where $\frac{\partial \phi}{\partial t}$ is the change in the porosity with time under the action of a compaction, swelling/dehydration, sorption, and chemical reaction. $\left(-\mathrm{p}_a \rho_c \frac{dm_b}{dt}\right)$ is the source term of CO_2. It is provided by the diffusion processes of free gas and absorption/adsorption process of adsorbed gas in the shale matrix (Appendix C). Similarly, $\left(-\rho_{bw} \frac{dm_{bw}}{dt}\right)$ is the water term. It is supplied by the dehydration of the matrix. p_a corresponds to the atmospheric pressure. $f'_{bw} = \rho_{bw} f_{bw}$ and $f'_{nw} = \beta f_{nw}$.

4.2. Navier Equation for Shale Deformation

For the elastic shale saturated by the CO_2 and brine water, the Navier equation for the deformation of the porous medium is [16]:

$$Gu_{i,jj} + \frac{G}{1-2\nu} u_{k,kj} = K(\varepsilon_{D,i} + \varepsilon_{s,i}) - \alpha \overline{p}_{,i} - f_i \tag{36}$$

where G is the shear modulus. $u_{i,jj}$ is the second-order derivative in the jth direction of the displacement in the ith direction u_i. ν is the Poisson's ratio. $\overline{p}_{,i}$ is the derivative of the pore pressure in the ith direction and calculated by $\overline{p} = S_w p_w + S_{nw} P_{nw}$. α is the Biot coefficient.

Equation (36) shows that there are four sources of the body force: the body force induced by dehydration-swelling ($K\varepsilon_{D,i}$), the body force induced by sorption-swelling ($K\varepsilon_{s,i}$), the friction force induced by the two-phase flow (drag force or $\alpha\overline{p}_{,i}$), and the body force induced by gravity (f_i). The resistance is decided by the Biot's coefficient, and the body force induced by the swelling of the skeleton is correlated with the bulk modulus.

5. Numerical Modelling for the Assessment of Caprock Sealing Efficiency

5.1. Verification of This fully Coupled Multi-Physical Model

The British Geological Survey has carried out a gas breakthrough test on the argillite in the Callovo-Oxfordian formation [46]. Figure 6 shows the sample for this breakthrough test whose dimension was 5.39 cm high and 2.72 cm wide. For the flow field, there was no flow at the two side walls. For the deformation field, the two walls were also fixed. Helium was slowly injected from the bottom of the caprock with the pressure increasing from 6.5 to 10.5 MPa in a series of increments. A constant backpressure of 4.5 MPa was applied at the top of the caprock, and a confining stress of 12.5 MPa was maintained through the experiment. Before the gas injection, the caprock was fully saturated by water. Water and helium were allowed to flow out from the top boundary at a constant pressure. Gerard et al. [46] completed the hydro-mechanical modeling with a preferential gas pathway. They proposed a continuous finite element matrix embedding a single fracture to describe this problem. This study uses their computational parameters except the capillary-saturation relationship. We also use our log–log relationship instead of their Van Genuchten relationship for the relative permeabilities. Those parameters which were not given by Gerard et al. [46] are taken from other publications or our estimation. Tables 1 and 2 summarize all the parameters in our computations. Because helium was used, no sorption and hydration were considered. In this proposed multi-physical model, the helium flow was only along the fracture network, thus no additional single fracture was required for the simulations. The flow rate of helium gas from the top boundary was calculated and compared with the experimental measurements. Our simulations considered two cases: the first case was a constant entry pressure of 2.1 MPa and the second case was a variable gas entry pressure which was evolving with the effective strain. The initial gas entry pressure was taken as $p_{ei} = 2.1$ MPa.

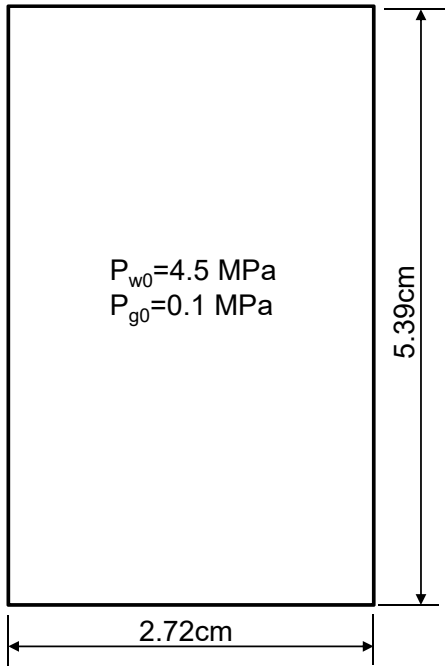

Figure 6. Geometry of breakthrough test problem.

Table 1. Langmuir pressure and strain in gas breakthrough test.

Relative Constant	Directions to the Bedding		
	Paralleling	Perpendicular	Average
Langmuir pressure p_L (MPa)	6.5	6.2	6.0
Langmuir strain ε_L (%)	1.5	3.7	2.7

Table 2. Computation parameters for gas breakthrough test.

Parameter	Unit	Value	Physical Meanings
s_{nwr}		0.05	Helium residual saturation
s_{bwr}		0.6	Water residual saturation
P_{ei}	MPa	2.1	Initial entry capillary pressure
μ_{bw}	Pa*s	0.00085	Water viscosity
μ_{nw}	Pa*s	2.0×10^{-5}	Helium viscosity
λ_{bw}		3	Water's Corey parameter
λ_{nw}		3	Helium's Corey parameter
λ		1.1	Pore size distribution index
T	K	300	Experimental temperature
p_{bw0}	MPa	4.5	Initial pressure of water
p_{nw0}	MPa	6.66	Initial pressure of helium
ϕ_0		0.18	Initial porosity
k_0	m^2	1.33×10^{-20}	Initial shale permeability
p_L	MPa	6	Langmuir pressure of helium
E_c	GPa	3.8	Overall Young's modulus of shale
E_s	GPa	9.5	Matrix Young's modulus of shale
ν		0.3	Poisson's ratio
ρ_c	kg/m^3	2300	Density of shale
k_{nwe}		0.005	Helium's relative permeability at end point
p_{nwout}	MPa	6.62	Outlet pressure of helium
p_{bwout}	MPa	4.5	Outlet pressure of water

Comparison between the experimental data and numerical simulations is shown in Figure 7. It is found that there are the same flow rates before the gas breakthrough

in either the constant or variable entry pressure cases. These flow rates before the gas breakthrough are very low and depend on the absolute permeability and the initial gas saturation. With the gas–water front moving to the top boundary, the sample deforms and the fracture aperture thus changes, particularly near the mixing zone of helium and water. This deformation changes the gas entry pressure. The case of variable gas entry pressure is observed to have an earlier gas breakthrough time and the rapid increase in the flow rate after the gas breakthrough. The case of a constant gas entry pressure has a much later gas breakthrough time and a much lower flow rate after the gas breakthrough. It is also shown that a variable gas entry pressure can better reproduce the experimental data. A good agreement is observed between the numerical results by the variable gas entry pressure in Equation (20) and the experimental observations. There is a single fracture in the computational domain of their model. However, only the flow in fracture network is described in our model, thus a single fracture is not required. This treatment largely extends the capacity of our model to handle large-scale problems for the evaluation of the caprock sealing efficiency.

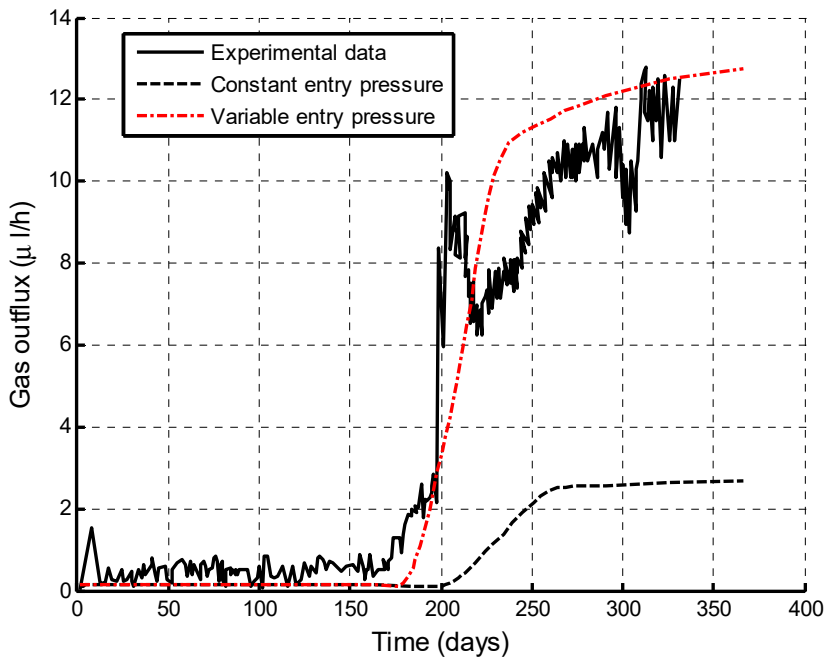

Figure 7. Comparison of gas outflux between experimental data [46] and our numerical simulations.

5.2. Impacts of Shale Matrix Dehydration on CO_2 Penetration

5.2.1. Model and Parameters

As shown in Figure 8, a typical geometric model of 10 m × 10 m was established for a one-dimensional penetration problem. For the flow field, there was no flow at the two side walls. However, CO_2 and brine water can flow out from the top boundary. For the deformation field, the two walls and bottom were constrained. The CO_2 was injected from the bottom with a given injection pressure. It increased from the reservoir pressure to 27 MPa in an exponential form and then remains constant for 1000 years. The diffusion time for both the CO_2 and brine water was taken as 1d. The computational parameters are shown in Table 3. The caprock contains 54.1% quartz, 25.6% kaolinite, 13.5% illite and mica, and 2.5% K-feldspar by weight. The dehydration-induced swelling is still described by Equation (7). In this example, the short-term interaction mechanism was studied in the CO_2–brine two-phase flow process. Furthermore, the impacts of the two-phase flow, the CO_2 sorption, and dehydration/swelling on the caprock sealing efficiency were comprehensively analyzed in the two-phase flow process.

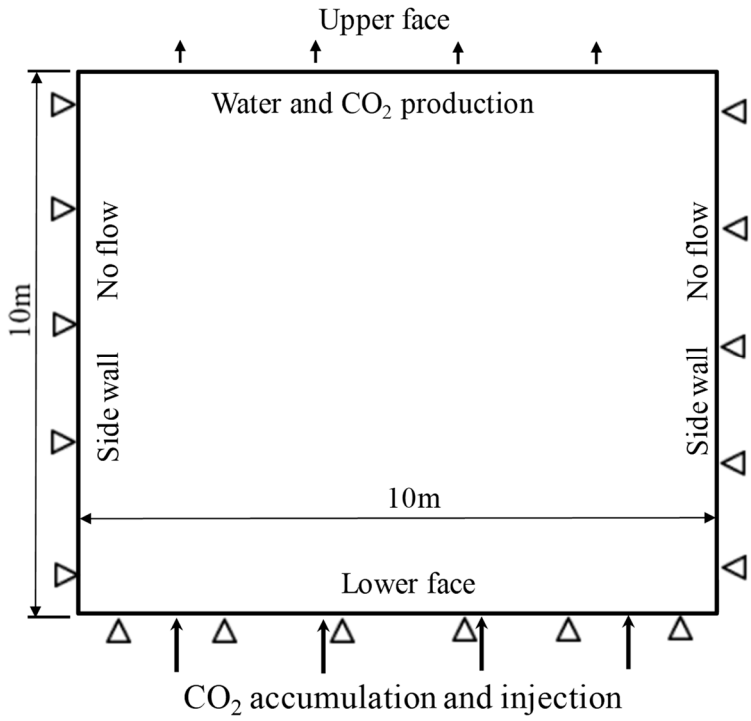

Figure 8. Numerical model for CO_2-water two-phase flow in caprock.

Table 3. Computation parameters for CO_2 penetration.

Parameter	Unit	Value	Physical Meanings
s_{nwr}		0.15	CO_2 residual saturation
s_{bwr}		0.6	Brine water residual saturation
P_{ei}	MPa	10	Capillary entry pressure at initial state
T	K	353.15	Temperature taken from CO_2 storage reservoirs
μ_{bw}	Pa*s	3.6×10^{-4}	Viscosity of brine water
μ_{nw}	Pa*s	5.2×10^{-5}	Viscosity of CO_2
λ_{bw}		6.5	Brine Water's Corey parameter
λ_{nw}		2.6	CO_2's Corey parameter
λ		2.0	Distribution index of pore size
p_{bwf}	MPa	8.95	Pressure at the top boundary
p_{bw0}	MPa	8.95	Water pressure at initial state
p_{nw0}	MPa	19	CO_2 pressure at initial state
ϕ_0		0.04	Initial porosity
k_0	m^2	1.5×10^{-19}	Initial permeability
p_L	MPa	6	CO_2 Langmuir pressure
V_L	m^3/kg	0.03	Shale Langmuir sorption capacity
E_c	GPa	8	Overall Young's modulus of shale
E_s	GPa	20	Matrix Young's modulus of shale
ν		0.30	Poisson's ratio
ρ_c	kg/m^3	2300	Density of shale
p_{nwout}	MPa	19	Outlet pressure of CO_2
p_{bwout}	MPa	8.95	Outlet pressure of brine water
D	m^2/s	1.2×10^{-11}	Coefficient of diffusion in shale
k_{rbw}^{max}		1.0	Brine water relative permeability at end point
k_{rnw}^{max}		0.015	CO_2 relative permeability at end point

5.2.2. Impacts of Matrix Dehydration on CO_2–Brine Displacement Process

The impacts of dehydration-induced shrinkage on the CO_2-water displacement are studied here. The two initial states of the shale matrix were assumed: a fully saturated with the dehydration (called dehydration) state and a fully saturated without the dehydration

(called the base case) state. The time of the numerical calculation was 317 years (10^{10} s). Figure 9 presents the effect of the matrix dehydration on the water saturation in the fracture network when the injection time is 317 years. It is noted that the shrinkage strain due to the dehydration is only specified as 15 % of the swelling strain. This figure shows that the dehydration of the shale matrix has a slight impact on the water saturation distribution in the vertical direction. In the CO_2–brine water two-phase flow process, two competitive factors result in the swelling or shrinkage of the shale matrix. Figure 10a presents the increase in the swelling strain induced by the CO_2 sorption with time. The observation point is located at 0.1 m away from the lower face. The CO_2 diffusion causes the swelling of the shale matrix. At the same time, the dehydration process makes the shale matrix shrink, as shown in Figure 10b. It is noted that the magnitude of the shrinkage strain is much smaller than the sorption-induced swelling strain in this example. The combination of the CO_2 sorption-induced swelling and the dehydration-induced shrinkage makes the permeability ratio slightly increase, then decrease, and finally reach a low value. Figure 11 presents the permeability evolution at the observation point. The dehydration process contributes a little to the increase in the early stage but significantly reduces the extent of self-limiting in the fracture network. This reduction in self-limiting is also observed from the vertical distribution of the permeability ratio at time of 3.17 years in Figure 12. The minimum permeability ratio is bigger due to dehydration. This implies that the dehydration increases the fracture apertures and thus alleviates the reduction in the permeability of the fracture network due to swelling. The impact of the dehydration on the penetration depth is shown in Figure 13. In this sense, the penetration depth with the dehydration is much higher than without the dehydration. Therefore, the risk of a gas breakthrough is increased due to the dehydration.

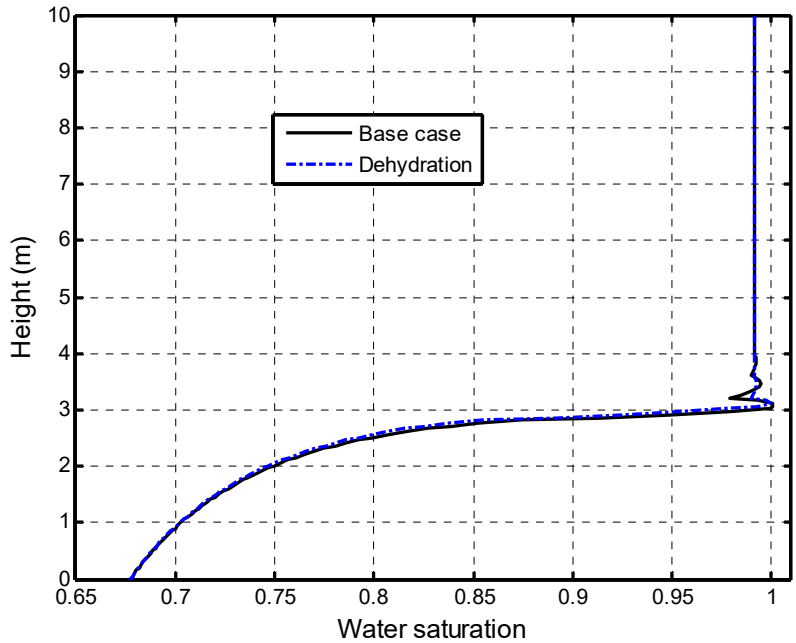

Figure 9. Effect of dehydration on the water saturation in fracture network at 317 years.

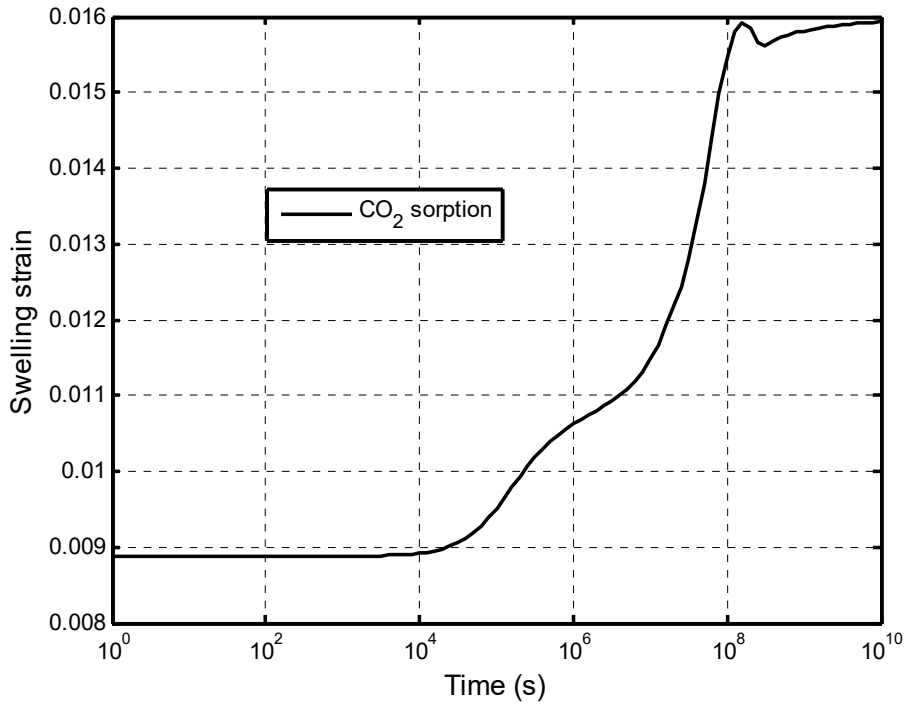

(**a**) CO_2 sorption-induced swelling strain

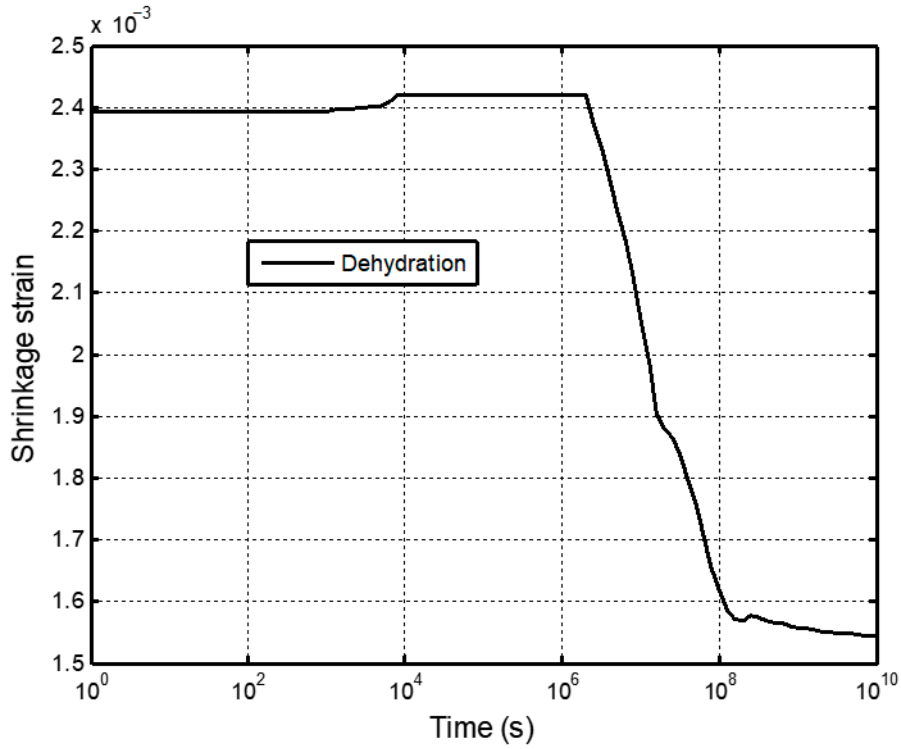

(**b**) Dehydration-induced strain shrinkage

Figure 10. Swelling/shrinkage strain induced by two competitive factors at the observation point.

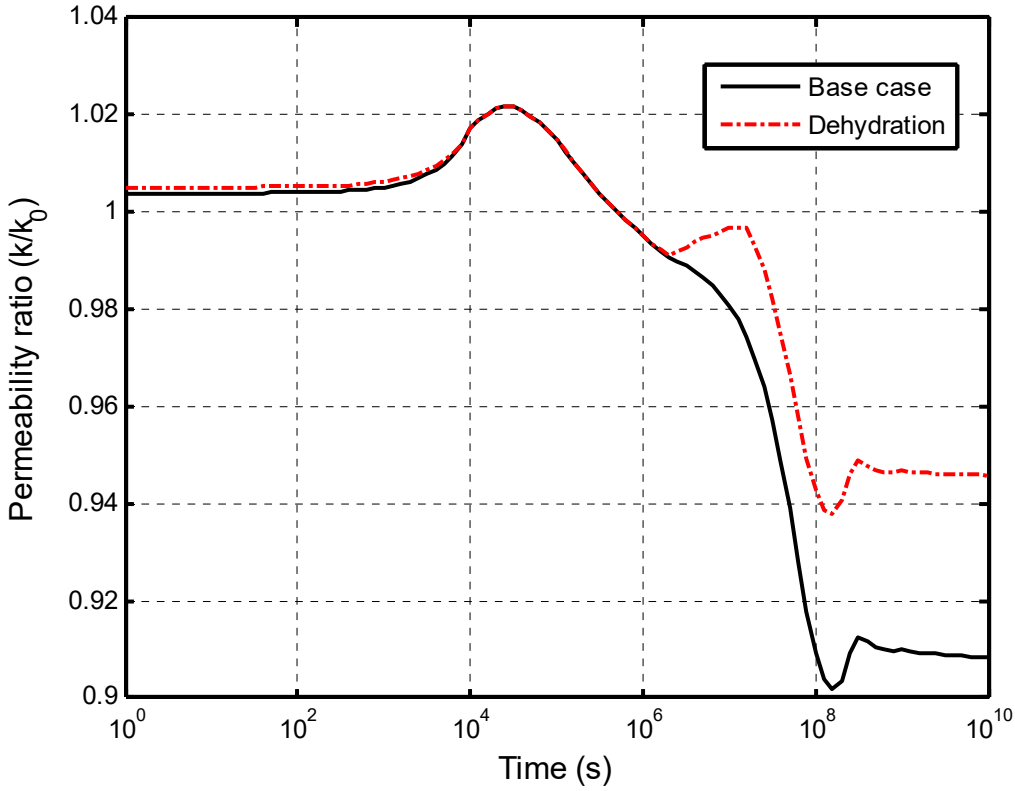

Figure 11. Comparations of permeability ratio at the observation point.

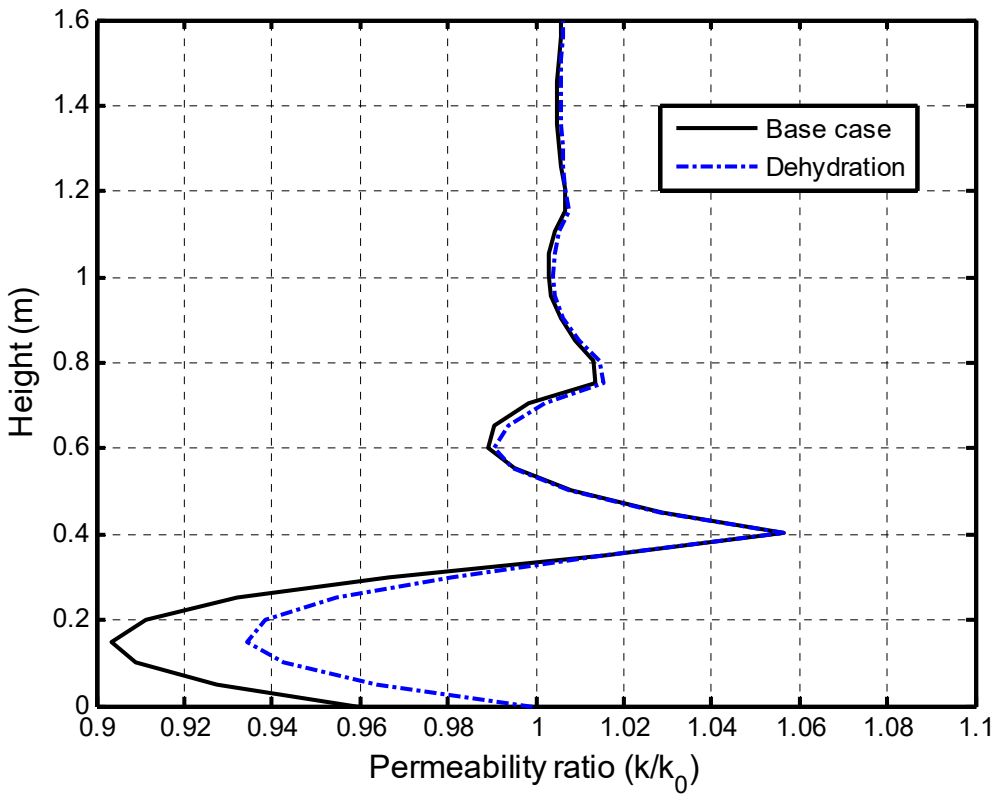

Figure 12. Comparations of permeability distribution in the vertical direction at 3.17 years.

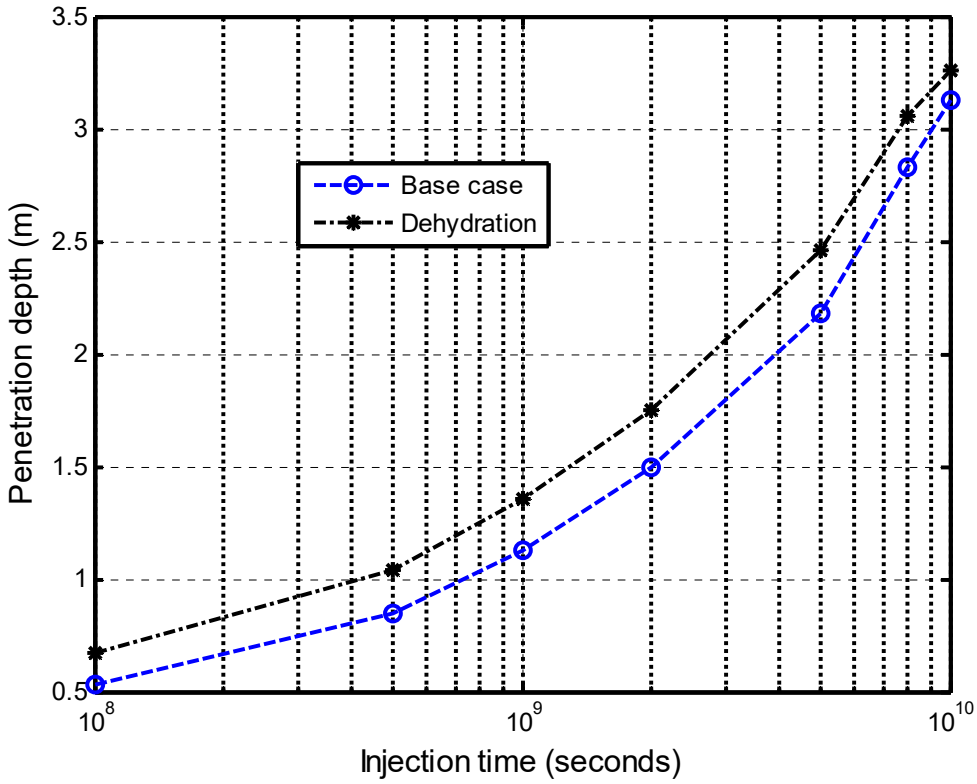

Figure 13. Effect of dehydration on the penetration depth.

5.2.3. Self-Limiting Mechanism Analysis

The self-limiting mechanism of caprock is complicated. This mechanism comes from the two competitions of the shale matrix swellings: the CO_2 sorption-induced swelling and the dehydration-induced shrinkage. As the flow paths narrow down and even close under the action of the swelling, the permeability in the fractures will decrease and the penetration speed of the CO_2–water front will slow down [47]. If the action of the swelling becomes stronger along the flow direction, the efficiency of the caprock sealing can be enhanced. For the initially water-saturated shale matrix, the CO_2 diffusion can induce the shale matrix dehydration [48]. This dehydration changes the water content and induces the shrinkage of the shale matrix. The fracture apertures get wider due to the shrinkage of the shale matrix during the CO_2 diffusion. The worst case is to reopen the flow channels which are closing due to a full swelling of the shale matrix under in situ conditions. Such an increase in the apertures increases the permeability and penetration depth [35]. This condition reduces the efficiency of the caprock sealing and there is a potential leakage risk of CO_2. Figure 12 shows that the permeability fluctuates and is different in the two-phase flow region or the sweeping zone which moves with the CO_2–water front. After the two-phase flow, the permeability decreases by about 10% along the flow direction for the base case and approximately 6% from the contribution of dehydration. In this regard, the dehydration process has an effect on the swelling strain. In addition, the self-limiting/enhancing capacity has also been influenced. On this sense, it can be concluded that the strong dehydration within the caprock can significantly influence the caprock sealing. For the water-saturated caprock, the CO_2 infiltration may cause the matrix dehydration [49]. Therefore, the caprock dehydration should be carefully considered in the evaluation of the caprock sealing.

6. Conclusions

A multi-physical coupling model was proposed to investigate the effects of dehydration and sorption on the efficiency of the caprock sealing. This model was further validated by a gas breakthrough test. The combined effects of CO_2 adsorption-induced swelling and dehydration-induced shrinkage on the permeability and entry capillary pressure of

the fracture network were studied through this model. Particularly, the impact of the dehydration-induced shrinkage on the penetration depth was particularly studied. The following conclusions can be drawn from these investigations:

First, this multi-physical coupling model is a sound tool for the assessment of the sealing efficiency of caprock. It includes the capacity of our previous model in illustrating the physical and mechanical properties of caprock, such as the compaction deformation, gas flow, and sorption. It also expands its capacity, including the dehydration of the shale matrix and the porosity and permeability evolution in the fracture network due to the dehydration shrinkage and compaction.

Second, the evolution mechanisms of the porosity and permeability are complicated and complex, particularly in the CO_2–brine two-phase flow region and the gas sweeping region. These evolutions are the interaction results among the CO_2 diffusion, mechanical compaction, two-phase flow, CO_2 sorption-induced swelling, and dehydration-induced shrinkage. These interactions cause the effects of self-enhancing/limiting in these regions due to a swelling/shrinkage of the shale matrix.

Finally, the sorption-induced swelling and dehydration-induced shrinkage in the saturated shale caprock are two competitive factors to alter the efficiency of caprock sealing. A CO_2 infiltration may cause the matrix's dehydration from the water-saturated caprock. This matrix dehydration can induce the re-opening of some fractures, enhance the permeability, and reduce the efficiency of caprock sealing, thus being a potential risk for CO_2 geological sequestration. Caprock dehydration is worthy of being carefully considered in the evaluation of the caprock sealing efficiency.

Author Contributions: Conceptualization, X.S. and J.W.; methodology, H.W.; software, X.S. and H.W.; validation, X.S., J.W. and X.W.; formal analysis, X.W.; investigation, J.W.; resources, J.W.; data curation, X.S.; writing—original draft preparation, X.S. and J.W.; writing—review and editing, H.W.; visualization, X.S.; supervision, J.W.; project administration, H.W.; funding acquisition, J.W. and X.S. All authors have read and agreed to the published version of the manuscript.

Funding: This research was funded by the National Natural Science Foundation of China (Grant No. 51674246, 52204113).

Institutional Review Board Statement: Not applicable.

Informed Consent Statement: Not applicable.

Data Availability Statement: Not applicable.

Conflicts of Interest: There are no conflict of interests to declare.

Appendix A. Capillary Pressure

The capillary pressure in this paper refers to the pressure difference between the CO_2 phase and the brine water phase:

$$p_c = p_{nw} - p_{bw} \tag{A1}$$

where p_c is the capillary pressure and p_{nw} and p_{bw} are the pressures of CO_2 and brine water, respectively.

Based on the Leverett J-function and the Corey–Brooks formula, the capillary pressure is expressed by:

$$p_c = p_e \sqrt{\frac{\phi}{k}} (s_w^*)^{-\frac{1}{\lambda}} \tag{A2}$$

The saturation of water is:

$$s_{bw} = s_{bw}^* (1 - s_{rnw} - s_{rbw}) + s_{bw} \tag{A3}$$

where p_e is the entry capillary pressure. s^*_{bw} is the normalized saturation of the brine water. s_{rbw} and s_{rnw} are the irreducible saturations for brine water and CO_2, respectively. λ is the distribution index of the pore sizes.

Therefore, the coefficient of the saturation with respect to the capillary pressure is:

$$C_p = \frac{\partial s_{bw}}{\partial p_c} = \frac{\partial s_{bw}}{\partial s^*_{bw}} \frac{\partial s^*_w}{\partial p_c} = (1 - s_{rbw} - s_{rnw}) \left(-\frac{\lambda}{p_e} (s^*_{bw})^{1+\frac{1}{\lambda}} \right) \sqrt{\frac{k}{\phi}} \tag{A4}$$

Appendix B. Relative Permeability Model in Fracture Network

The relative permeability can be expressed by a relationship between the capillary pressure and the effective gas permeability as the previous models for two-phase flow in shales and mudstones [50]:

$$k_{rbw} = k^{max}_{rbw} (s^*_{bw})^{\lambda_{bw}} \tag{A5}$$

$$k_{rnw} = k^{max}_{rnw} (s^*_{nw})^{\lambda_{nw}} \tag{A6}$$

$$s^*_w = 1 - s^*_{nw}, \quad s^*_{nw} = \frac{s_{nw} - s_{nwi}}{1 - s_{nwi}} \tag{A7}$$

where k^{max}_{rbw} and k^{max}_{rnw} are the endpoint relative permeabilities for brine water and CO_2, respectively. s_{bwi} and s_{nwi} are the irreducible saturations for brine water and CO_2, respectively. λ_{bw} and λ_{nw} are the reference parameters with relative permeabilities.

Appendix C. Gas Absorption and Sorption-Induced Swelling in Matrix

The CO_2 adsorbed content is defined as:

$$m_e = \frac{V_L p}{p_L + p} \tag{A8}$$

where m_e is the adsorbed content of CO_2 and p is the pressure of CO_2. V_L and P_L are the Langmuir volume constant and Langmuir pressure, respectively.

The sorption-induced swelling strain is denoted by:

$$\varepsilon_s = \frac{\varepsilon_L p}{p_L + p} \tag{A9}$$

where ε_s is the swelling strain induced by sorption and ε_L refers to the Langmuir strain.

Both m_e and ε_s are related with the confining pressure and temperature. They also vary with the shale burial condition.

References

1. Vialle, S.; Druhan, J.L.; Maher, K. Multi-phase flow simulation of CO_2, leakage through a fractured caprock in response to mitigation strategies. *Int. J. Greenh. Gas Control* **2016**, *44*, 11–25. [CrossRef]
2. Hardisty, P.E.; Sivapalan, M.; Brooks, P. The Environmental and Economic Sustainability of Carbon Capture and Storage. *Int. J. Environ. Res. Public Health* **2011**, *8*, 1460–1477. [CrossRef] [PubMed]
3. Dalkhaa, C.; Shevalier, M.; Nightingale, M.; Mayer, B. 2-D reactive transport modeling of the fate of CO_2 injected into a saline aquifer in the Wabamun Lake Area, Alberta, Canada. *Appl. Geochem.* **2013**, *38*, 10–23. [CrossRef]
4. Zhou, Q.; Birkholzer, J.T. On scale and magnitude of pressure build-up induced by large-scale geologic storage of CO_2. *Greenh. Gases.* **2015**, *1*, 11–20. [CrossRef]
5. MacMinn, C.W.; Juanes, R. Post-injection spreading and trapping of CO_2 in saline aquifers: Impact of the plume shape at the end of injection. *Comput. Geosci.* **2009**, *13*, 483–491. [CrossRef]
6. Hou, L.H.; Yu, Z.C.; Luo, X.; Wu, S.T. Self-sealing of caprocks during CO_2 geological sequestration. *Energy* **2022**, *252*, 124064. [CrossRef]
7. Matter, J.M.; Kelemen, P.B. Permanent storage of carbon dioxide in geological reservoirs by mineral carbonation. *Nat. Geosci.* **2009**, *2*, 837–841. [CrossRef]
8. Lee, S.; Fischer, T.B.; Stokes, M.R.; Klingler, R.J.; Ilavsky, J.; McCarty, D.K.; Wigand, M.O.; Derkowski, A.; Winans, R.E. Dehydration effect on the pore size, porosity, and fractal parameters of shale rocks: Ultrasmall-angle X-ray scattering study. *Energy Fuels* **2014**, *28*, 6772–6779. [CrossRef]

9. Iglauer, S.; Al-Yaseri, A.Z.; Rezaee, R.; Lebedev, M. CO_2 wettability of caprocks: Implications for structural storage capacity and containment security. *Geophys. Res. Lett.* **2016**, *42*, 9279–9284. [CrossRef]
10. Boait, F.C.; White, N.J.; Bickle, M.J.; Chadwick, R.A.; Neufeld, J.A.; Huppert, H.E. Spatial and temporal evolution of injected CO_2 at the Sleipner feld, North Sea. *J. Geophys. Res.* **2012**, *117*, B03309.
11. Abdelouahab, A.; Abdelhakim, B. CO_2-storage assessment and effective capacity in Algeria. *Springerplus* **2016**, *5*, 1038.
12. Kivi, I.R.; Makhnenko, R.Y.; Vilarrasa, V. Two-Phase Flow Mechanisms Controlling CO_2 Intrusion into Shaly Caprock. *Transp. Porous Med.* **2022**, *141*, 771–798. [CrossRef]
13. Bickle, M.; Chadwick, A.; Huppert, H.E.; Hallworth, M.; Lyle, S. Modelling carbon dioxide accumulation at Sleipner: Implications for underground carbon storage. *Earth Planet. Sc. Lett.* **2007**, *255*, 164–176. [CrossRef]
14. Heath, J.E.; Dewers, T.A.; McPherson, B.J.O.L.; Nemer, M.B.; Kotula, P.G. Pore-lining phases and capillary breakthrough pressure of mudstone caprocks: Sealing efficiency of geologic CO_2 storage sites. *Int. J. Greenh. Gas Control* **2012**, *11*, 204–220. [CrossRef]
15. Zhang, C.; Wang, M.L. A critical review of breakthrough pressure for tight rocks and relevant factors. *J. Nat. Gas Sci. Eng.* **2022**, *100*, 104456. [CrossRef]
16. Wang, J.G.; Peng, Y. Numerical modeling for the combined effects of two-phase flow, deformation, gas diffusion and CO_2 sorption on caprock sealing efficiency. *J. Geochem. Explor.* **2014**, *144*, 154–167. [CrossRef]
17. Espinoza, D.N.; Santamarina, J.C. CO_2 breakthrough—Caprock sealing efficiency and integrity for carbon geological storage. *Int. J. Greenh. Gas Control* **2017**, *66*, 218–229. [CrossRef]
18. Roshan, H.; Ehsani, S.; Marjo, C.E.; Andersen, M.S.; Acworth, R.I. Mechanisms of water adsorption into partially saturated fractured shales: An experimental study. *Fuel* **2015**, *159*, 628–637. [CrossRef]
19. Ewy, R.T. Shale swelling/shrinkage and water content change due to imposed suction and due to direct brine contact. *Acta Geotech.* **2014**, *9*, 869–886. [CrossRef]
20. Shang, X.J.; Wang, J.G.; Zhang, Z.Z.; Gao, F. A three-parameter permeability model for the cracking process of fractured rocks under temperature change and external loading. *Int. J. Rock Mech. Min.* **2019**, *123*, 104106. [CrossRef]
21. Vega, B.; Dutta, A.; Kovscek, A.R. CT imaging of low-permeability, dual-porosity systems using high X-ray contrast gas. *Transp. Porous Med.* **2014**, *101*, 81–97. [CrossRef]
22. Liu, J.; Wang, J.G.; Gao, F.; Ju, Y.; Tang, F. Impact of micro- and macro-scale consistent flows on well performance in fractured shale gas reservoirs. *J. Nat. Gas Sci. Eng.* **2016**, *36*, 1239–1252. [CrossRef]
23. Zhang, K.Q.; Jin, Z.J.; Li, S.Y. Coupled miscible carbon utilization-storage processes in fractured shales. *Chem. Eng. J.* **2022**, *441*, 135987. [CrossRef]
24. Wang, J.G.; Ju, Y.; Gao, F.; Peng, Y.; Gao, Y. Effect of CO_2 anisotropic sorption and swelling on caprock sealing efficiency. *J. Clean. Prod.* **2015**, *103*, 685–695. [CrossRef]
25. Lyu, Q.; Ranjith, P.G.; Long, X.; Kang, Y.; Huang, M. A review of shale swelling by water adsorption. *J. Nat. Gas Sci. Eng.* **2015**, *27*, 1421–1431. [CrossRef]
26. War, K.; Raveendran, G.; Arnepalli, D.N. Coupled hydromechanical model for evaluating the volume change and fluid permeation behavior of expansive clay smear in a fault upon interaction with CO_2. *Int. J. Greenh. Gas Control* **2022**, *119*, 103696. [CrossRef]
27. Ougier-Simonin, A.; Renard, F.; Boehm, C.; Vidal-Gilbert, S. Microfracturing and microporosity in shales. *Earth-Sci. Rev.* **2016**, *162*, 198–226. [CrossRef]
28. Rohmer, J.; Tremosa, J.; Marty, N.C.M.; Audigane, P. Modelling of the CO_2-induced degradation of a fractured caprock during leakage: Potential for a mechanical self-limiting process. *Rock Mech. Rock Eng.* **2017**, *50*, 2763–2783. [CrossRef]
29. Liu, C.; Hoang, S.K.; Tran, M.H.; Abousleiman, Y.N.; Ewy, R.T. Poroelastic dual-porosity dual-permeability simulation of pressure transmission test on chemically active shale. *J. Eng. Mech.* **2017**, *143*, 04017016. [CrossRef]
30. Kassa, A.M.; Gasda, S.E.; Landa-Marb'an, D.; Sandve, T.H.; Kumar, K. Field-scale impacts of long-term wettability alteration in geological CO_2 storage. *Int. J. Greenh. Gas Control* **2022**, *114*, 103556. [CrossRef]
31. Wang, K.; Xu, T.; Wang, F.; Tian, H. Experimental study of CO_2 –brine–rock interaction during CO_2, sequestration in deep coal seams. *Int. J. Coal Geol.* **2016**, *154–155*, 265–274. [CrossRef]
32. Gao, F.; Liu, J.; Wang, J.G.; Ju, Y. Impact of micro-scale heterogeneity on gas diffusivity of organic-rich shale matrix. *J. Nat. Gas Sci. Eng.* **2017**, *45*, 75–87. [CrossRef]
33. Chareonsuppanimit, P.; Mohammad, S.A.; Robinson, R.L.; Gasem, K.A.M. High-pressure adsorption of gases on shales: Measurements and modelling. *Int. J. Coal Geol.* **2012**, *95*, 34–46. [CrossRef]
34. Bai, G.; Zhou, Z.J.; Li, X.M.; Cheng, Y.T.; Hu, K.; Chen, Y.; Zhou, X.H. Quantitative analysis of carbon dioxide replacement of adsorbed methane in different coal ranks using low-field NMR technique. *Fuel* **2022**, *326*, 124980. [CrossRef]
35. Wang, J.G.; Ju, Y.; Gao, F.; Liu, J. A simple approach for the estimation of CO_2 penetration depth into a caprock layer. *J. Rock Mech. Geotech.* **2016**, *8*, 75–86. [CrossRef]
36. Broseta, D.; Tonnet, N.; Shah, V. Are rocks still water-wet in the presence of dense CO_2 or H_2S? *Geofluids* **2012**, *12*, 280–294. [CrossRef]
37. Edvardsen, L.; Bhuiyan, M.H.; Cerasi, P.R.; Bjorge, R. Fast evaluation of caprock strength sensitivity to different CO_2 solutions using small sample techniques. *Rock Mech. Rock Eng.* **2021**, *54*, 6123–6133. [CrossRef]

38. Mouzakis, K.M.; Navarre-Sitchler, A.K.; Rother, G.; Banuelos, J.L.; Wang, X.Y.; Kaszuba, J.P.; Heath, J.E.; Miller, Q.R.S.; Alvarado, V.; McCray, J.E. Experimental study of porosity changes in shale caprocks exposed to CO_2-saturated brines I: Evolution of mineralogy, pore connectivity, pore size distribution, and surface Area. *Environ. Eng. Sci.* **2016**, *33*, 725–735. [CrossRef]
39. Fatah, A.; Bennour, Z.; Ben Mahmud, H.; Gholami, R.; Hossain, M.M. A review on the influence of CO_2/shale interaction on shale properties: Implications of CCS in shales. *Energies* **2020**, *13*, 3200. [CrossRef]
40. Liu, J.Y.; Wang, S.; Javadpour, F.; Feng, Q.H.; Cha, L.M. Hydrogen diffusion in clay slit: Implications for the geological storage. *Energy Fuels* **2022**, *36*, 7651–7660. [CrossRef]
41. Brown, K.M.; Ransom, B. Porosity corrections for smectite-rich sediments: Impact on studied of compaction, fluid generation, and tectonic history. *Geology* **1996**, *24*, 843–846. [CrossRef]
42. Yew, C.H.; Chenevert, M.E.; Wang, C.L.; Osisanya, S.O. Wellbore stress distribution produced by moisture adsorption. *SPE Drill. Eng.* **1990**, *5*, 311–316. [CrossRef]
43. Rabbani, H.S.; Joekarniasar, V.; Shokri, N. Effects of intermediate wettability on entry capillary pressure in angular pores. *J. Colloid Interf. Sci.* **2016**, *473*, 34–43. [CrossRef] [PubMed]
44. Zhang, C.; Oostrom, M.; Grate, J.W.; Wietsma, T.W.; Warner, M. Liquid CO_2 displacement of water in a dual-permeability pore network micromodel. *Environ. Sci. Technol.* **2011**, *45*, 7581–7588. [CrossRef] [PubMed]
45. Gholami, M.; Talaie, M.R.; Roodpeyma, S. Mathematical modeling of gas dehydration using adsorption process. *Chem. Eng. Sci.* **2010**, *65*, 5942–5949. [CrossRef]
46. Gerard, P.; Harrington, J.; Charlier, R.; Collin, F. Hydro-mechanical modeling of the development of preferential gas pathways in claystone. In *Unsaturated Soils: Research and Applications*; Springer Press: Berlin, Germany, 2012; pp. 175–180.
47. Yang, K.; Zhou, J.P.; Xian, X.F.; Zhou, L.; Zhang, C.P.; Tian, S.F.; Lu, Z.H.; Zhang, F.S. Chemical-mechanical coupling effects on the permeability of shale subjected to supercritical CO_2-water exposure. *Energy* **2022**, *248*, 123591. [CrossRef]
48. Wang, J.S.; Samara, H.; Jaeger, P.; Ko, V.; Rodgers, D.; Ryan, D. Investigation for CO_2 adsorption and wettability of reservoir rocks. *Energy Fuels* **2022**, *36*, 1626–1634. [CrossRef]
49. Sang, G.J.; Liu, S.M. Carbonate caprock-brine-carbon dioxide interaction: Alteration of hydromechanical properties and implications on carbon dioxide leakage. *SPE J.* **2021**, *26*, 2780–2792. [CrossRef]
50. Bachu, S.; Bennion, B. Effects of in-situ conditions on relative permeability characteristics of CO_2-brine systems. *Environ. Geol.* **2008**, *54*, 1707–1722. [CrossRef]